


RESEARCH ARTICLE | JANUARY 31 2019

# Liquid crystal enabled dynamic cloaking of terahertz Fano resonators

Zhi-Xiong Shen; Sheng-Hang Zhou; Shi-Jun Ge; Wei Hu ; Yan-Qing Lu*Appl. Phys. Lett.* 114, 041106 (2019)<https://doi.org/10.1063/1.5082224>

## Articles You May Be Interested In

Acoustically induced transparency using Fano resonant periodic arrays

*J. Appl. Phys.* (October 2015)

Integrative implementation of scattering reduction and radiation enhancement for an electrically small antenna by subwavelength plasmas

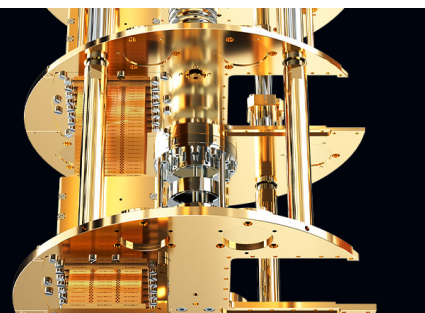
*Phys. Plasmas* (July 2024)

Tuning of Fano resonances in terahertz metamaterials

*J. Appl. Phys.* (February 2015) **BLUE  
FORS**

### Accelerate your research.

Scale up your experiments with increased cooling power and a new side-loading LD system.

[Discover the latest advances in cooling](#)

# Liquid crystal enabled dynamic cloaking of terahertz Fano resonators

Cite as: Appl. Phys. Lett. **114**, 041106 (2019); doi: [10.1063/1.5082224](https://doi.org/10.1063/1.5082224)

Submitted: 20 November 2018 · Accepted: 21 January 2019 · Published Online: 31 January 2019



View Online



Export Citation



CrossMark

Zhi-Xiong Shen,<sup>1,2</sup> Sheng-Hang Zhou,<sup>1</sup> Shi-Jun Ge,<sup>1,2</sup> Wei Hu,<sup>1,2,a)</sup>  and Yan-Qing Lu<sup>1,b)</sup>

## AFFILIATIONS

<sup>1</sup> National Laboratory of Solid State Microstructures, Key Laboratory of Intelligent Optical Sensing and Manipulation, Collaborative Innovation Center of Advanced Microstructures, College of Engineering and Applied Sciences, Nanjing University, Nanjing 210093, China

<sup>2</sup> Institute for Smart Liquid Crystals, JITRI, Changshu 215500, China

<sup>a)</sup> Electronic mail: [huwei@nju.edu.cn](mailto:huwei@nju.edu.cn).

<sup>b)</sup> Electronic mail: [yqlu@nju.edu.cn](mailto:yqlu@nju.edu.cn).

## ABSTRACT

Terahertz (THz) metadevices featured by high-Q Fano resonance are applicable for ultrasensitive biodetection. The active tuning of Fano resonance further extends their applications to switching and filtering. Here, we propose a dynamic Fano cloaking in a liquid crystal (LC) integrated THz metasurface. The metasurface is composed of two-gap asymmetric split rings. Its Fano resonance is intensively dependent on the incident polarization. The Fano resonance occurs when illuminated by THz waves with polarization perpendicular to the gaps, while for parallel polarization, the Fano resonance vanishes, namely, the cloaking of Fano resonators. A 250- $\mu\text{m}$ -thick LC layer functions as an integrated tunable polarization converter. Thus, the device can be electrically switched between the sharp Fano state and the high-transmission state. The modulation depth reaches over 50% in a broad frequency range of 660 GHz. This work may inspire various advanced active THz apparatuses for biosensing, switching, and filtering.

Published under license by AIP Publishing. <https://doi.org/10.1063/1.5082224>

The terahertz (THz) technology is a rapidly developing field with great potential in security screening, biomedicine, and wireless communication.<sup>1,2</sup> The collective vibrational modes of various biomolecules oscillate in this range, which results in unique THz fingerprints, facilitating the real time THz biodetection.<sup>2,3</sup> The sensitivity of biodetection could be enhanced via introducing high-Q resonances. Metasurfaces featured by Fano resonance can perfectly satisfy the above requirement.<sup>4</sup> Fano resonance originates from the coherent coupling between a discrete narrow resonance and a continuous broad one.<sup>5</sup> Metasurfaces, periodic artificial electromagnetic media structured on a subwavelength and two-dimensional scale, reveal remarkable capability for THz wave manipulations.<sup>6</sup> To introduce Fano resonance into metasurfaces, a structural asymmetry is usually adopted in the unit.<sup>7</sup> Such metasurfaces are able to generate large electromagnetic field confinement and exhibit a sharp and asymmetric spectrum.

Once the above metasurfaces are fabricated, their geometry is fixed, and thus, the resonant wavelength and functions

remain static. This restricts their practical application in active and multifunctional apparatuses. To address this issue, functional materials, such as semiconductors (e.g., silicon<sup>8</sup> and perovskite<sup>9</sup>) and two-dimensional materials (e.g., graphene<sup>10</sup> and MoS<sub>2</sub><sup>11</sup>), are integrated with metasurfaces to realize active tuning of Fano resonance. The conductivity change induced by the external bias or optical pump leads to the tuning of Fano resonators. However, such devices suffer from a minor modulation depth and a narrow modulation frequency range. Therefore, further exploiting active Fano resonance with a broadband large modulation depth is urgent and meaningful. Liquid crystals (LCs) possess broadband birefringence with pronounced electro-tunability. Corresponding LC devices, including phase shifters,<sup>12</sup> waveplates,<sup>13,14</sup> vortex generators,<sup>15</sup> and active filters,<sup>16</sup> are widely investigated and developed in the THz range. Since the LC waveplate can act as a dynamic polarization converter, it may supply a practical strategy to realize active and large tuning of Fano resonance via integrating LC with incident polarization sensitive metasurfaces.

In this paper, we propose an active terahertz Fano resonator and demonstrate it by integrating an LC polarization converter with a metallic metasurface composed of two-gap asymmetric split rings (ASRs). In the bias OFF state, the device presents a sharp Fano resonance. When a saturated bias is applied, a high-transmission spectrum arises. The voltage is applied through two few-layer graphene electrodes, and thus, the device can be freely switched between the Fano resonance state and the high-transmission state. It enables the dynamic cloaking of Fano resonators within a broadband frequency range. The proposed design may inspire various active functional THz apparatuses.

The configuration of the device is illustrated in Fig. 1(a). Both the superstrate and the substrate are 500- $\mu\text{m}$ -thick fused silica and separated by a 250- $\mu\text{m}$ -thick Mylar spacer. The substrate is covered with an Au metasurface composed of a two-gap ASR array. The micrograph of the metasurface is shown in Fig. 1(b). A 2- $\mu\text{m}$ -thick PDMS film is coated on the metasurface to separate the metasurface from the electrode, in order to avoid the short circuit of ASR resonators. Few-layer graphene is chosen as the transparent electrodes. Both substrates are spin-coated with a sulfonic azo dye (SD1) alignment layer<sup>17</sup> to induce the LC orientation to be  $45^\circ$  with respect to the  $x$  axis. A large-birefringence home-made LC NJU-LDn-4<sup>18</sup> with an average birefringence over 0.30 from 0.80 to 2.80 THz is infiltrated. LC orientations in bias OFF and saturated states are schematically illustrated in Figs. 1(c) and 1(d), respectively.

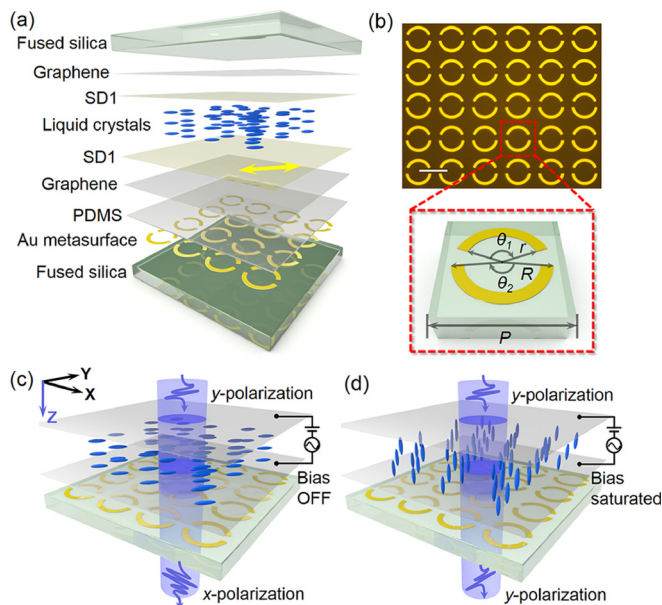


**FIG. 1.** (a) The schematic illustration of the active terahertz metadvice. The yellow arrow indicates the alignment direction. (b) The micrograph of the Fano resonators. The scale bar indicates 50  $\mu\text{m}$ . The inset in (b) shows the ASR unit dimension: lattice periodicity,  $p$ : 60  $\mu\text{m}$ ; inner radius,  $r$ : 18  $\mu\text{m}$ ; outer radius,  $R$ : 24  $\mu\text{m}$ ; shorter arc angle,  $\theta_1$ :  $136^\circ$ ; and longer arc angle,  $\theta_2$ :  $166^\circ$ . (c) and (d) The LC orientations in (c) bias OFF and (d) bias saturated states.

The metasurface is fabricated using the standard photolithography technique. The fused silica substrate is ultrasonically bathed in alcohol and O-plasma treated for 10 min. A 1.5  $\mu\text{m}$  positive photoresist SF6 film and a 1.5  $\mu\text{m}$  AZ5214 film are successively coated on the substrate. Such a bilayer configuration facilitates the lift-off process. Masks consisting of desired patterns are aligned and exposed to UV light after prebaking at  $115^\circ\text{C}$ . After developing, electron beam evaporation is applied to deposit 200 nm Au. Finally, samples are soaked in acetone to lift off the undesired Au. The obtained metasurface is spin-coated at 5000 r.p.m. for 30 s with PDMS (sylgard 184 silicone elastomer, Dow Corning). Then, the PDMS covered metasurface and a bare substrate are transferred with few-layer graphene from copper foil (Six Carbon Technology, Shenzhen, China). Afterwards, they are spin-coated at 3000 r.p.m. for 30 s with SD1 (Dainippon Ink and Chemicals Inc., Chiba, Japan) solution dissolved in N, N-dimethylformamide (DMF). The two substrates are assembled with a 250- $\mu\text{m}$ -thick Mylar spacer to form a cell. After exposing under a linearly polarized 405 nm blue LED of  $3\text{ J}/\text{cm}^2$  for 10 min, the LC is infiltrated and homogeneously aligned.

The performance of the metasurface is distinguishable for the incident polarization perpendicular ( $x$ -polarization) and parallel ( $y$ -polarization) to the ASR gap. The simulated and measured transmission and phase spectra are presented in Figs. 2(a) and 2(b), respectively. For  $x$ -polarization, two pronounced resonant peaks arise. A sharp peak and a broad one are observed at 1.50 THz and 2.00 THz, respectively [Fig. 2(a)]. To describe the resonant mechanism, the simulated current density and electric field of single unit at 1.50 THz and 2.00 THz are revealed in Figs. 2(c)–2(f). As illustrated in Fig. 2(c), the induced surface currents at 1.50 THz are anti-parallel in the up and down arcs, suggesting a magnetic dipole moment perpendicular to the  $xy$ -plane. The electric field at 1.50 THz reveals a large electromagnetic field confinement on both edges of the arcs [Fig. 2(d)]. The above facts indicate that the narrow resonance originates from the

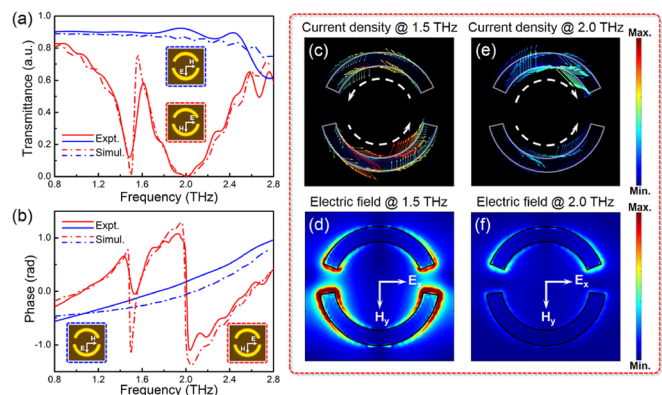


**FIG. 2.** (a) Numerical simulations and measured transmission spectra of the metasurface when the incident wave is  $x$ -polarized (red curve) and  $y$ -polarized (blue curve). (b) Corresponding phase spectra with  $x$ -polarization (red curve) and  $y$ -polarization (blue curve). The simulated (c) and (e) current density and (d) and (f) electric field of single unit at 1.50 THz and 2.00 THz with  $x$ -polarization, respectively. The white dashed arrows in (c) and (e) depict the directions of induced surface currents.

subradiant dark mode and the radiation losses are suppressed due to the weak coupling to free space. For the resonance at 2.00 THz, the currents in Fig. 2(e) are parallel in the up and down arcs, indicating a dipole resonance. The electric field in Fig. 2(f) is much weaker compared to that in Fig. 2(d), revealing a high radiative loss caused by the strong coupling between resonators and free space. Thus, a broad resonant peak appears at 2.00 THz. These two resonances interfere with each other to form the high-Q Fano resonance. The phase spectrum reveals the corresponding dispersive properties at 1.50 THz and 2.00 THz. A deviation of the resonant linewidth (Q) and intensity (I) occurs at 1.50 THz between the simulation ( $Q = 11.70$ ;  $I = 0.74$ ) and the measurement ( $Q = 9.90$ ;  $I = 0.46$ ), as shown in Fig. 2(a). This is mainly attributed to the imperfect fabrication of the metasurface and limited time window of the measurement. The cutoff of the time window is necessary to remove the influence of the Fabry-Perot echo. Here, the structure asymmetry is 9.93% calculated by  $(\theta_2 - \theta_1)/(\theta_2 + \theta_1)$ . Actually, when the structure asymmetry decreases, the Q-factor increases exponentially, while the intensity of Fano resonance decreases sharply as well, leading to difficulties in both fabrication and the measurement. For practical applications, the product of the Q-factor and Fano intensity is expected to be maximized, and thereby, a tradeoff between the Q-factor and Fano intensity should be considered.<sup>19</sup> For y-polarization, the Fano resonance is cloaked and a non-resonant spectrum is observed from 0.80 to 2.80 THz.

All the numerical simulations are carried out using Lumerical FDTD Solutions. The metasurface is set as a conductive material with a DC conductivity of  $4.09 \times 10^7$  S/m. The refractive index of the substrate and the PDMS layer is set as 1.92 and 1.60, respectively. A 250- $\mu\text{m}$ -thick anisotropic medium with a refractive index of  $n_o = 1.50 + i0.006$  and  $n_e = 1.80 + i0.001$  is placed between the superstrate and the substrate. The LC orientation module is applied to simulate the optical properties of the metadvice along with the variation of LC directors.

The LC waveplate is electrically driven to switch the incident polarization. Unlike the metasurface waveplate which exhibits a relatively low efficiency due to resonant nature, the LC waveplate is non-resonant and shows a relatively high efficiency in a broadband.<sup>20</sup> Here, we choose the few-layer graphene as the electrode, which exhibits pronounced conductivity and high transmittance in the THz band.<sup>21</sup> As both the Fano resonance peak at 1.50 THz and the dipole resonance peak at 2.00 THz are designed to be cloaked [see Fig. 2(a)], we optimize the LC thickness to be 250  $\mu\text{m}$  to achieve the half-wave condition at 1.75 THz. The performance of the LC waveplate is characterized using THz time-domain spectroscopy<sup>22</sup> (THz-TDS, TAS7400SP; Advantest Corporation, Tokyo, Japan) with a transmission polarization analysis module. Figure 3(a) schematically illustrates the experimental setup. It is composed of three metal grating polarizers (P). P1 and P3 are fixed parallelly, with grating vectors orientated along the y-axis to select y-polarization, whereas the grating vector of P2 can be set to  $45^\circ$  or  $-45^\circ$  with respect to the y-axis. The LC orientation is  $45^\circ$  with respect to the y-axis. After passing through the waveplate, the ordinary ( $E_o$ ) and extraordinary ( $E_e$ ) components of the THz wave are

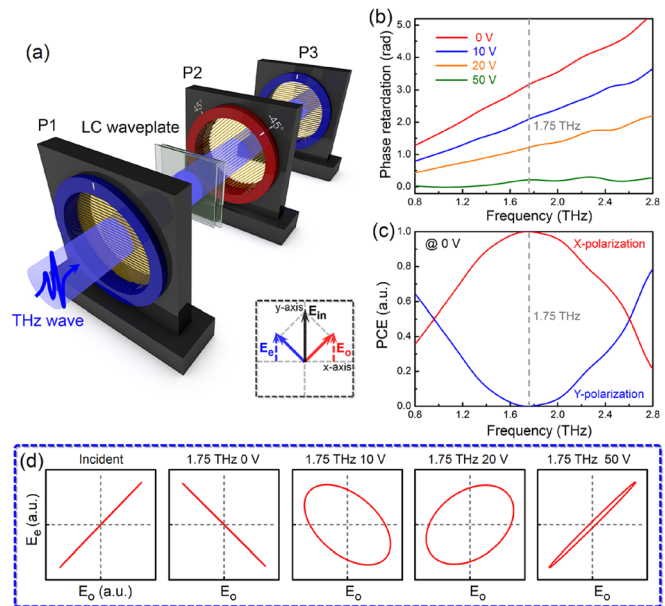


**FIG. 3.** (a) Schematic setup of the transmission polarization analysis module of the THz-TDS. The inset depicts the incident y-polarization (labeled as  $E_{in}$ ) and two orthogonal polarizations (labeled as  $E_e$  and  $E_o$ ) in the measurement. (b) Frequency-dependent phase retardation at different bias values. (c) Frequency-dependent polarization conversion efficiency (PCE) at 0 V. (d) The incident polarization and polarization evolution from 0 V to 50 V at 1.75 THz.

detected. The phase retardation between them is obtained by  $\delta\varphi = 2\pi\delta n d/\lambda$ , where  $\delta n$  is the birefringence,  $d$  is the cell gap, and  $\lambda$  is the incident wavelength. The waveplate is driven by a 1 kHz square-wave alternating voltage signal. Figure 3(b) exhibits the phase retardation at different bias values. As the bias increases from 0 V to 50 V, LCs gradually stand up and finally orient along the z-axis, contributing to a decrease in  $\delta n$  and subsequent  $\delta\varphi$ . The tuning of  $\delta\varphi$  causes the evolution of output polarizations. When  $\delta\varphi = \pi$ , the incident y-polarization is converted to x-polarization. Figure 3(c) reveals the frequency-dependent polarization conversion efficiency (PCE) at 0 V. A complete y- to x-polarization conversion occurs at 1.75 THz. The incident polarization and polarization evolution at 1.75 THz induced by the electrical tuning (0 V to 50 V) of the LC waveplate is presented in Fig. 3(d), which shows a continuous polarization conversion.

We utilize the same THz-TDS setup to characterize the performance of the LC integrated metadvice. Figure 4(a) reveals the measured transmission spectra at 0 V, 10 V, 20 V, and 50 V. As the voltage rises up, the Fano peak gradually converts to a non-resonant spectrum due to the change of incident polarization. The calculated LC orientations at 0 V, 10 V, 20 V, and 50 V are  $0^\circ$ ,  $32^\circ$ ,  $50^\circ$ , and  $90^\circ$  with respect to the xy-plane, respectively.<sup>23</sup> The corresponding simulated transmission spectra are exhibited in Fig. 4(b), which match well with the experimental results. The measured width and amplitude ( $Q = 9.90$ ;  $I = 0.20$ ) of the resonant peak at 1.30 THz differ slightly with simulation ( $Q = 15.20$ ;  $I = 0.29$ ) at 0 V, which might be attributed to the



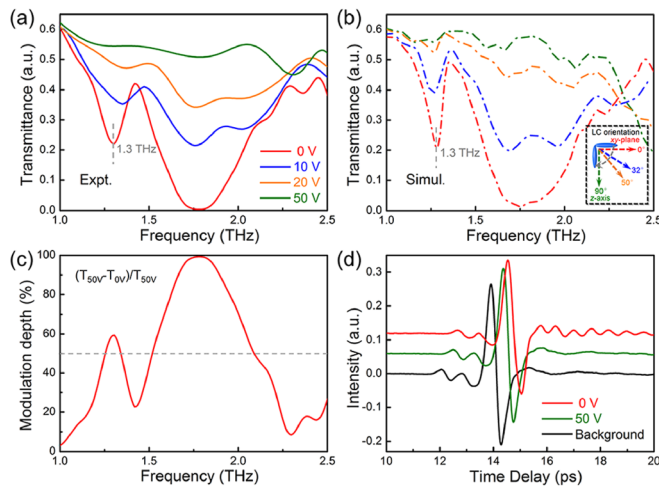


**FIG. 4.** (a) Measured transmission spectra of the device at 0 V, 10 V, 20 V, and 50 V. (b) Simulated transmission spectra of the device when the LC orientation is 0°, 32°, 50°, and 90° with respect to the xy-plane. (c) Modulation depth spectrum calculated from the experimental results. (d) Measured time-domain THz pulse after passing through the fused silica substrate and the device at bias of 0 V and 50 V.

deviation of LC orientations between simulation and reality. Compared to a similar structure that integrates LCs and the plasmonic metasurface in the NIR band to achieve mode-switching between bias ON and OFF states,<sup>24</sup> our device can be continuously tuned with bias. Also, not like the visible or NIR range, LC orientation in the THz band is not influenced by the frameworks of the metasurface, which adds freedom to LC orientation and consequent functions of the device. The modulation depth is obtained by  $(T_{50V} - T_{0V})/T_{50V}$  and presented in Fig. 4(c). It is obvious that a large modulation depth (over 50%) covers broad frequency bands (from 1.25 THz to 1.34 THz and 1.52 THz to 2.09 THz), which could be further enhanced by optimizing the metasurface geometry or adopting larger-birefringence LCs. The feature of the broadband large modulation depth makes the device promising in active switching and filtering. In Fig. 4(d), we exhibit the time-domain THz pulse after passing through the fused silica substrate (labelled as background) and the device biased at 0 V and 50 V. A vibrated tail with a long duration time after the main THz pulse is observed at 0 V, indicating the slow light behaviors in the high-Q Fano resonance,<sup>25</sup> while at 50 V, the vibrated tail disappears and the pulse becomes similar to that of the background. This means that the Fano resonance is cloaked, which is consistent with the non-resonant spectrum in the frequency domain. It is noticed that there is a time delay difference among the three THz pulses. This is attributed to the different phase shift of the samples. The response time of the device is relatively long (in the second scale) due to the large LC thickness in the THz range. Via stacking several cells, the tuning speed could be greatly improved.<sup>14</sup> The traditional way to control the polarization is rotating a pair of polarizers to extract the required linear polarization component. This method suffers from two shortcomings. First, mechanical rotators are necessary, causing it bulky and costly.

Second, the insertion loss is significant and the intensity changes with rotation, and thus, calibration is unavoidable. The proposed LC waveplate is able to actively tune the polarization by an external bias. The device is very compact with no moving part, therefore satisfying the minimization and integration tendencies of THz apparatuses.

In summary, we develop an LC integrated THz metadvice. Through electrically controlling the LC orientations, active tuning of functions is realized. A sharp Fano resonance is exhibited in the bias OFF state, while the Fano resonance is distinctly cloaked in the bias saturated state. The device shows the merits of broadband large modulation depth, thus providing a promising way for fabricating active high-Q THz apparatuses that may be widely utilized in THz biodetecting, imaging, switching, and filtering.

This work was supported by the National Key Research and Development Program of China (2017YFA0303700), the National Natural Science Foundation of China (NSFC) (Nos. 61575093, 61490714, and 61435008), the Distinguished Young Scholars Fund of Jiangsu Province (BK20180004), the Fundamental Research Funds for the Central Universities, and Jiangsu Donghai Silicon Industry Science and Technology Innovation Center. W. H. gratefully acknowledges the support of the Tang Scholar program.

## REFERENCES

- <sup>1</sup>B. Ferguson and X. C. Zhang, *Nat. Mater.* **1**, 26 (2002); S. Koenig, D. Lopez-Diaz, J. Antes, F. Boes, R. Henneberger, A. Leuther, A. Tzschernig, R. Schmogrow, D. Hillerkuss, R. Palmer, T. Zwick, C. Koos, W. Freude, O. Ambacher, J. Leuthold, and I. Kallfass, *Nat. Photonics* **7**, 977 (2013).
- <sup>2</sup>K. Kawase, Y. Ogawa, Y. Watanabe, and H. Inoue, *Opt. Express* **11**, 2549 (2003).
- <sup>3</sup>W. Xu, L. Xie, and Y. Ying, *Nanoscale* **9**, 13864 (2017).
- <sup>4</sup>Y. Zhang, T. Li, B. Zeng, H. Zhang, H. Lv, X. Huang, W. Zhang, and A. K. Azad, *Nanoscale* **7**, 12682 (2015); L. Cong, Y. K. Srivastava, and R. Singh, *Appl. Phys. Lett.* **111**, 081108 (2017); R. Singh, W. Cao, I. Al-Naib, L. Cong, W. Withayachumnankul, and W. Zhang, *Appl. Phys. Lett.* **105**, 171101 (2014).
- <sup>5</sup>U. Fano, *Phys. Rev.* **124**, 1866 (1961); B. Luk'yanchuk, N. I. Zheludev, S. A. Maier, N. J. Halas, P. Nordlander, H. Giessen, and C. T. Chong, *Nat. Mater.* **9**, 707 (2010); M. F. Limonov, M. V. Rybin, A. N. Poddubny, and Y. S. Kivshar, *Nat. Photonics* **11**, 543 (2017).
- <sup>6</sup>N. Yu and F. Capasso, *Nat. Mater.* **13**, 139 (2014); H. Zhang, X. Zhang, Q. Xu, C. Tian, Q. Wang, Y. Xu, Y. Li, J. Gu, Z. Tian, C. Ouyang, X. Zhang, C. Hu, J. Han, and W. Zhang, *Adv. Opt. Mater.* **6**, 1700773 (2018); L. Gao, Q. Cheng, J. Yang, S. Ma, J. Zhao, S. Liu, H. Chen, Q. He, W. Jiang, H. Ma, Q. Wen, L. Liang, B. Jin, W. Liu, L. Zhou, J. Yao, P. Wu, and T. Cui, *Light Sci. Appl.* **4**, e324 (2015); Q. Wang, X. Zhang, Y. Xu, Z. Tian, J. Gu, W. Yue, S. Zhang, J. Han, and W. Zhang, *Adv. Opt. Mater.* **3**, 779 (2015); Q. Wang, X. Zhang, E. Plum, Q. Xu, M. Wei, Y. Xu, H. Zhang, Y. Liao, J. Gu, J. Han, and W. Zhang, *Adv. Opt. Mater.* **5**, 1700277 (2017).
- <sup>7</sup>R. Singh, I. A. I. Al-Naib, M. Koch, and W. Zhang, *Opt. Express* **19**, 6312 (2011); W. Cao, R. Singh, I. A. I. Al-Naib, M. He, A. J. Taylor, and W. Zhang, *Opt. Lett.* **37**, 3366 (2012).
- <sup>8</sup>M. Manjappa, Y. K. Srivastava, L. Cong, I. Al-Naib, and R. Singh, *Adv. Mater.* **29**, 1603355 (2017); J. Gu, R. Singh, X. Liu, X. Zhang, Y. Ma, S. Zhang, S. A. Maier, Z. Tian, A. K. Azad, H. Chen, A. J. Taylor, J. Han, and W. Zhang, *Nat. Commun.* **3**, 1151 (2012).
- <sup>9</sup>L. Cong, Y. K. Srivastava, A. Solanki, T. C. Sum, and R. Singh, *ACS Photonics* **4**, 1595 (2017).
- <sup>10</sup>Z. X. Chen, J. H. Chen, Z. J. Wu, W. Hu, X. J. Zhang, and Y. Q. Lu, *Appl. Phys. Lett.* **104**, 161114 (2014); N. K. Emani, T. Chung, A. V. Kildishev, V. M. Shalaev, Y. P. Chen, and A. Boltasseva, *Nano Lett.* **14**, 78 (2014).

- <sup>11</sup>Y. K. Srivastava, A. Chaturvedi, M. Manjappa, A. Kumar, G. Dayal, C. Kloc, and R. Singh, *Adv. Opt. Mater.* **5**, 1700762 (2017).
- <sup>12</sup>X. Lin, J. Wu, W. Hu, Z. Zheng, Z. Wu, G. Zhu, F. Xu, B. Jin, and Y. Lu, *AIP Adv.* **1**, 032133 (2011); Y. Y. Ji, F. Fan, M. Chen, L. Yang, and S. J. Chang, *Opt. Express* **25**, 11405 (2017).
- <sup>13</sup>C. Hsieh, R. Pan, T. Tang, H. Chen, and C. Pan, *Opt. Lett.* **31**, 1112 (2006).
- <sup>14</sup>L. Wang, X. Lin, W. Hu, G. Shao, P. Chen, L. Liang, B. Jin, P. Wu, H. Qian, Y. Lu, X. Liang, Z. Zheng, and Y. Lu, *Light Sci. Appl.* **4**, e253 (2015).
- <sup>15</sup>S. J. Ge, P. Chen, Z. X. Shen, W. F. Sun, X. K. Wang, W. Hu, Y. Zhang, and Y. Q. Lu, *Opt. Express* **25**, 12349 (2017).
- <sup>16</sup>D. Shrekenhamer, W. Chen, and W. J. Padilla, *Phys. Rev. Lett.* **110**, 177403 (2013); Z. Shen, S. Zhou, S. Ge, W. Duan, P. Chen, L. Wang, W. Hu, and Y. Lu, *Opt. Lett.* **43**, 4695 (2018).
- <sup>17</sup>P. Chen, L. Ma, W. Duan, J. Chen, S. Ge, Z. Zhu, M. Tang, R. Xu, W. Gao, T. Li, W. Hu, and Y. Lu, *Adv. Mater.* **30**, 1705865 (2018).
- <sup>18</sup>L. Wang, X. Lin, X. Liang, J. Wu, W. Hu, Z. Zheng, B. Jin, Y. Qin, and Y. Lu, *Opt. Mater. Express* **2**, 1314 (2012).
- <sup>19</sup>L. Cong, M. Manjappa, N. Xu, I. Al-Naib, W. Zhang, and R. Singh, *Adv. Opt. Mater.* **3**, 1537 (2015).
- <sup>20</sup>X. Zhao, J. Schalch, J. Zhang, H. R. Seren, G. Duan, R. D. Averitt, and X. Zhang, *Optica* **5**, 303 (2018).
- <sup>21</sup>Y. Wu, X. Ruan, C. Chen, Y. J. Shin, Y. Lee, J. Niu, J. Liu, Y. Chen, K. Yang, X. Zhang, J. Ahn, and H. Yang, *Opt. Express* **21**, 21395 (2013); L. Wang, S. Ge, W. Hu, M. Nakajima, and Y. Lu, *Opt. Express* **25**, 23873 (2017).
- <sup>22</sup>M. C. Nuss and J. Orenstein, *Millimeter and Submillimeter Wave Spectroscopy of Solids* (Springer, Berlin, Heidelberg, 1998).
- <sup>23</sup>X. Lin, W. Hu, X. Hu, X. Liang, Y. Chen, H. Cui, G. Zhu, J. Li, V. Chigrinov, and Y. Lu, *Opt. Lett.* **37**, 3627 (2012).
- <sup>24</sup>M. Decker, C. Kremers, A. Minovich, I. Staude, A. E. Miroshnichenko, D. Chigrin, D. N. Neshev, C. Jagadish, and Y. S. Kivshar, *Opt. Express* **21**, 8879 (2013).
- <sup>25</sup>J. Wu, B. Jin, J. Wan, L. Liang, Y. Zhang, T. Jia, C. Cao, L. Kang, W. Xu, J. Chen, and P. Wu, *Appl. Phys. Lett.* **99**, 161113 (2011).